The Astronomical Journal, 166:246 (16pp), 2023 December https://doi.org/10.3847/1538-3881/ad05cf

CD –27°11535: Evidence for a Triple System in the β Pictoris Moving Group

Andrew D. Thomas[1,2], Eric L. Nielsen[1,3], Robert J. De Rosa[4], Anne E. Peck[3], Bruce Macintosh[1,5,6], Jeffrey Chilcote[7], Paul Kalas[8], Jason J. Wang[9,10,11], Sarah Blunt[9,12], Alexandra Greenbaum[13], Quinn M. Konopacky[14], Michael J. Ireland[15], Peter Tuthill[16], Kimberly Ward-Duong[17], Lea A. Hirsch[18], Ian Czekala[19,20,21,22,23,28], Franck Marchis[24], Christian Marois[25,26], Max A. Millar-Blanchaer[27], William Roberson[1], Adam Smith[3], Hannah Gallamore[3], and Jessica Klusmeyer[3]

[1] Kavli Institute for Particle Astrophysics and Cosmology, Stanford University, Stanford, CA 94305, USA
[2] Seattle Sounders FC, 800 Occidental Avenue S, Seattle, WA 98134, USA
[3] Department of Astronomy, New Mexico State University, P.O. Box 30001, MSC 4500, Las Cruces, NM 88003, USA
[4] European Southern Observatory, Alonso de Córdova 3107, Vitacura, Santiago, Chile
[5] University of California Observatories, 1156 High Street, Santa Cruz, CA 95064, USA
[6] Department of Astronomy and Astrophysics, University of California, Santa Cruz, Santa Cruz, CA 95064, USA
[7] Department of Physics and Astronomy, University of Notre Dame, 225 Nieuwland Science Hall, Notre Dame, IN 46556, USA
[8] Department of Astronomy, University of California, Berkeley, Berkeley, CA 94720, USA
[9] Center for Interdisciplinary Exploration and Research in Astrophysics (CIERA), Northwestern University, Evanston, IL 60208, USA
[10] Department of Physics and Astronomy, Northwestern University, Evanston, IL 60208, USA
[11] Department of Astronomy, California Institute of Technology, Pasadena, CA 91125, USA
[12] Cahill Center for Astronomy & Astrophysics, California Institute of Technology, Pasadena, CA 91125, USA
[13] IPAC, Mail Code 100-22, Caltech, 1200 E. California Boulevard, Pasadena, CA 91125, USA
[14] Center for Astrophysics and Space Sciences, University of California, San Diego, La Jolla, CA 92093, USA
[15] Research School of Astronomy & Astrophysics, Australian National University, Canberra, ACT 2611, Australia
[16] Sydney Institute for Astronomy, University of Sydney, Physics Road, NSW 2006, Australia
[17] Department of Astronomy, Smith College, Northampton, MA 01063 USA
[18] Department of Chemical & Physical Sciences, University of Toronto Mississauga, Mississauga, ON L5L 1C6, Canada
[19] Department of Astronomy and Astrophysics, 525 Davey Laboratory, The Pennsylvania State University, University Park, PA 16802, USA
[20] Center for Exoplanets and Habitable Worlds, 525 Davey Laboratory, The Pennsylvania State University, University Park, PA 16802, USA
[21] Center for Astrostatistics, 525 Davey Laboratory, The Pennsylvania State University, University Park, PA 16802, USA
[22] Institute for Computational & Data Sciences, The Pennsylvania State University, University Park, PA 16802, USA
[23] Department of Astronomy, 501 Campbell Hall, University of California, Berkeley, Berkeley, CA 94720-3411, USA
[24] SETI Institute, 339 Bernardo Ave., Suite 200, Mountain View, CA 94043, USA
[25] National Research Council of Canada, Herzberg Astronomy and Astrophysics, 5071 West Saanich Road, Victoria, BC, V9E 2E7, Canada
[26] University of Victoria, 3800 Finnerty Road, Victoria, BC V8P 5C2, Canada
[27] Department of Physics, University of California, Santa Barbara, Santa Barbara, CA 93106, USA
Received 2023 March 20; revised 2023 October 15; accepted 2023 October 18; published 2023 November 15

Abstract

We present new spatially resolved astrometry and photometry of the CD –27°11535 system, a member of the β Pictoris moving group consisting of two resolved K-type stars on a ∼20 yr orbit. We fit an orbit to relative astrometry measured from NIRC2, GPI, and archival NaCo images, in addition to literature measurements. However, the total mass inferred from this orbit is significantly discrepant from that inferred from stellar evolutionary models using the luminosity of the two stars. We explore two hypotheses that could explain this discrepant mass sum: a discrepant parallax measurement from Gaia due to variability, and the presence of an additional unresolved companion to one of the two components. We find that the ∼20 yr orbit could not bias the parallax measurement, but that variability of the components could produce a large-amplitude astrometric motion, an effect that cannot be quantified exactly without the individual Gaia measurements. The discrepancy could also be explained by an additional star in the system. We jointly fit the astrometric and photometric measurements of the system to test different binary and triple architectures for the system. Depending on the set of evolutionary models used, we find an improved goodness of fit for a triple system architecture that includes a low-mass ($M = 0.177 \pm 0.055\ M_{\odot}$) companion to the primary star. Further studies of this system will be required in order to resolve this discrepancy, either by refining the parallax measurement with a more complex treatment of variability-induced astrometric motion or by detecting a third companion.

Unified Astronomy Thesaurus concepts: Astrometry (80); Stellar masses (1614); Young stellar objects (1834); Multiple stars (1081); Orbit determination (1175)

1. Introduction

Knowing the precise age of stars is essential to understanding the planets they host. The age of a star, especially a star evolving toward the zero-age main sequence, can be found using evolutionary models based on its mass and absolute luminosity, if the mass is measured independently. As the stars in moving groups formed at the same time, the age of one star

[28] NASA Hubble Fellowship Program Sagan Fellow.

Table 1
Parameters of CD-27

Parameter	Value	Reference
Alternate names	TYC 6820-223-1	
	Gaia DR2/3 4107812485571331328	
	WDS 17151−2750	
	ELP 40	
Position		1
R.A.	17:15:03.61 ± 0.26 mas	
Decl.	−27:49:39.74 ± 0.19 mas	
Proper motion (mas yr^{-1})	4.531 ± 0.447, −45.822 ± 0.297	1
Parallax (mas)	12.0040 ± 0.2854	1
Apparent magnitudes		
B	11.68 ± 0.12	2
V	10.596 ± 0.063	3
G	10.091995 ± 0.004247	4
I	9.129 ± 0.032	3
J	8.174 ± 0.029	5
H	7.537 ± 0.033	5
K_s	7.384 ± 0.031	5
Spectral type	K5Ve	

References: (1) Gaia Collaboration et al. (2018); (2) Høg et al. (2000); (3) Kiraga (2012); (4) Gaia Collaboration et al. (2021); (5) Cutri et al. (2003).

provides an estimate of the age of the whole group, especially when the moving group is young (Zuckerman & Song 2004; Bell et al. 2015; Schlieder et al. 2016). Exoplanet formation and brown dwarf evolution are closely related to those of its host star. Hence, knowing the age of a moving group can reveal the age of various exoplanets and brown dwarfs in it. These accurate ages allow us to constrain evolutionary models for exoplanet and brown dwarfs (Burgasser & Blake 2009) or simply lead to a better understanding of the formation of specific substellar objects. Binary stars provide the opportunity to discover the mass of the system through direct observation of the orbit. Fitting for the orbit reveals the dynamical total mass, which, in turn, reveals the age (Nielsen et al. 2016).

CD –27°11535 (CD-27) is a young K5 star and member of the β Pictoris (β Pic) moving group (Torres et al. 2006), with a Gaia Data Release 2 (DR2) distance of ∼83.3 pc (Gaia Collaboration et al. 2018). Further parameters of the star are described in Table 1. CD-27 was first identified as a young star by Torres et al. (2006) as part of the Search for Associations Containing Young stars (SACY) database, the aim of which was to determine space motion of young stars through radial velocity (RV), derived from spectroscopic observations. The spectroscopic observations also allowed them to determine the spectral type and equivalent width of Li λ6708, which can be used to suggest the age of the star (Carlos et al. 2016). For CD-27, they report an equivalent width of 490 mÅ for lithium—certainly indicating youth.

Age estimates of the CD-27 system of 6 Myr by Weise et al. (2010) and 10 Myr by Elliott et al. (2014) both reference the lithium equivalent width measurement by Torres et al. (2006). While an equivalent width of 490 mÅ does indicate an extremely young age (Stanford-Moore et al. 2020), a confounding factor is stellar multiplicity, which can affect the interpretation of such a measurement. Following its identification as a young star by Torres et al. (2006), Song et al. (2012) obtained new spectra and associated the star with the Upper Scorpius subgroup of the Scorpius-Centaurus (Sco-Cen) complex, though they note that the star may be a nearby nonmember. Later, Elliott et al. (2014) used RV measurements to approximate the systemic velocity and employ the convergence method of kinematic trace-back by Torres et al. (2006) to determine group membership. They conclude that CD-27 is a candidate member of β Pic, a doubt that stems from the uncertainty in the systemic velocity without an orbital solution. This is further studied by Shkolnik et al. (2017), who assign β Pic group membership by their confirmation criteria based on spectral type, proper motion, Li and Hα equivalent widths, and RV measurements. Age estimates of the β Pic moving group by Nielsen et al. (2016) suggest an age of 26 ± 3 Myr; as such, we expect that of CD-27 to be similar.

CD-27 was first identified as a binary by Elliott et al. (2014), who noted a significant RV difference measured by Torres et al. (2006) and Song et al. (2012) (−6.4 ± 1.0 and −1.1 ± 1.8 km s^{-1}, respectively), suggesting that the system is a single-lined spectroscopic binary. Their analysis yielded an RV of −6.9 ± 1.4 km s^{-1}, closer to the value reported by Torres et al. (2006) but significantly different than the −12.3 ± 3.2 km s^{-1} reported by Gaia Data Release 2 (DR2; Gaia Collaboration et al. 2018). Elliott et al. (2015) subsequently resolved the system with adaptive optics (AO) observations with an angular separation of 0.″08, listing the system as "AB, SB1." Alonso-Floriano et al. (2015), citing Elliott et al. (2015), list the system as an AaAb-B triple system, though it is unclear whether this is based on additional data not in either paper, or a misreading of the "AB, SB1" notation. More recently, Bonavita et al. (2022) as part of the SpHere INfrared Exoplanet (SHINE) project, also studied the CD-27 system. They fit an orbit to their relative astrometric measurements, yielding a total mass of the system of 2.14 ± 0.27 $M_\odot$, ∼1.5σ larger than their expectation for the total mass of the two stars of 1.75–1.82 $M_\odot$ from evolutionary models, depending on the age.

Our investigation into the CD-27 system was initially intended to provide another benchmark system for the β Pic moving group, utilizing the method outlined by Nielsen et al. (2016) and Montet et al. (2015) to further constrain the age of the association. However, the significant discrepancy between the total mass from the orbit and the masses derived from the luminosity of each component and evolutionary models precluded this analysis. Instead, we explored two scenarios that could explain this discrepancy. We begin with a description of the high angular resolution imaging observations of the system in Section 2, which we combined with literature measurements to fit an orbit to the relative astrometry in Section 3. We consider the possibility of an additional component within the system and the possibility of an incorrect distance determination in Section 4. We derive limits on the presence of an additional companion in Section 5, and we give conclusions and possible next steps for further studies in Section 6.

2. Observations and Data Reduction

To constrain the visual orbit of CD-27, we obtained diffraction-limited images of the system with the Keck/NIRC2 (PI: K. Matthews) and Gemini-S/GPI (Macintosh et al. 2014) instruments. We complemented these observations with archival data sets from Very Large Telescope (VLT)/NaCo (Lenzen et al. 2003; Rousset et al. 2003). In total, we collected

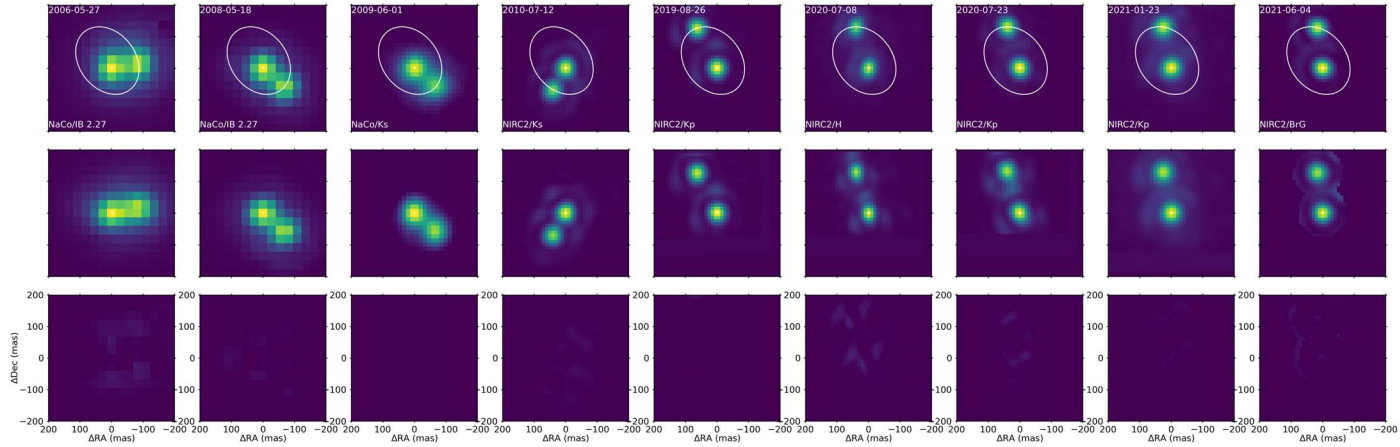

Figure 1. CD-27 for our nine epochs of imaging data, excluding the two GPI epochs. Along the top row are the initial reduced images, the middle row displays the model created using a PSF star, and the bottom row shows the results of the PSF fitting and subtraction of the model. The best-fit orbit (white) is displayed on the reduced images. The labels at the top of each column indicate the epoch, while those at the bottom of the reduced image list the instrument and filter.

18 observations on 11 separate epochs. The NaCo and NIRC2 observations were obtained in a conventional imaging mode, whereas the GPI observations were obtained with a non-redundant aperture mask (Greenbaum et al. 2019). A summary of these imaging observations is given in Table 4. We also obtained high-resolution optical echelle spectra of the system with APO/ARCES (Wang et al. 2003) as a part of a larger RV monitoring program.

2.1. VLT/NaCo Imaging

Observations of CD-27 that were made between 2006 May 27 and 2009 June 1 with the NaCo instrument were obtained from the ESO Science Archive Facility.[29] Two data sets were obtained with the S27 camera (27 mas pixel^{-1}) and the IB2.27 intermediate-band filter, and one was obtained with the S13 camera (13 mas pixel^{-1}) and the K_s broadband filter. These data were obtained under program IDs 077.C-0483, 081.C-0825, and 083.C-0659. The first two epochs were originally published in Elliott et al. (2015); however, the large uncertainty of their separation measurements motivated us to reanalyze their observations.

We used a standard near-infrared data reduction process to reduce and analyze each data set using associated calibrations obtained from the archive. The dark current was measured by finding the median of several exposures of the same exposure time taken while the instrument light path was blocked. This combined frame was then subtracted from each raw image. We created a flat field and bad pixel map using pairs of lamp-on and lamp-off exposures obtained during the day. These were used to perform the flat-field correction of the raw images and to correct for bad pixels. We did not apply any distortion correction to the image, as the effect of distortion over such a small angular separation between the two resolved components of the CD-27 system is negligible. The thermal background within each image was estimated using a median combination of all images, which was then subtracted from each image.

Relative astrometric and photometric measurements were made by fitting the point-spread function (PSF) of both components with that of a single star observed on the same (or neighboring) night with the same instrument configuration. We searched the archive for suitable observations for each of our three data sets. Unlike for CD-27, the individual images for the reference stars were aligned and combined to create a high signal-to-noise ratio (S/N) PSF that could be used for PSF fitting. The centroid of the star in each image was calculated by fitting a two-dimensional Gaussian within a region of 4 pixels centered on an initial guess for the location of the star. This process was repeated using the result of the first iteration as the guess position for the second.

A model of the two components of the CD-27 system was constructed using two copies of the model PSF interpolated to the positions (x_0, y_0) and (x_1, y_1) and multiplied by scaling factors f_0 and f_1. A background term (A) was added to account for any residual background signal present in the image. We used the implementation of Powell's method within the `scipy.optimize` package to find the optimal set of parameters that minimized the residuals after model subtraction in two $1.5\lambda/D$ apertures centered on the positions of the two components. This was repeated for each of the potential PSF calibrator stars. The PSF star that resulted in the smallest-amplitude residuals was used to measure the relative astrometry and photometry between the resolved components.

The pixel positions of the two components were converted into an angular separation and position angle using the plate scale and orientation of the detector given in Table 5. Magnitude differences were calculated from the ratio of the two scaling factors. This process was repeated for each image of the CD-27 system, yielding an average and standard deviation for each value that are given in Table 5. The reduced images, the best-fit PSF model, and the corresponding residuals are shown in Figure 1.

2.2. Keck/NIRC2 Imaging

The system was observed on six separate epochs over the course of 11 yr with Keck/NIRC2 through seven different filters (z, J, H, K_s, K', L', BrG). A single star was observed with the same filter that could act as a PSF reference in all but the last epoch in 2021 June. For that epoch, a PSF was constructed using the binary 1RXS J195602.8–320720 after digitally masking the fainter secondary. The observations were reduced using a standard near-infrared reduction pipeline similar to that employed to reduce the NaCo data. The raw images were dark subtracted, divided by a flat field, and cleaned of bad pixels using outlier rejection. The geometric distortion of the detector

[29] http://archive.eso.org

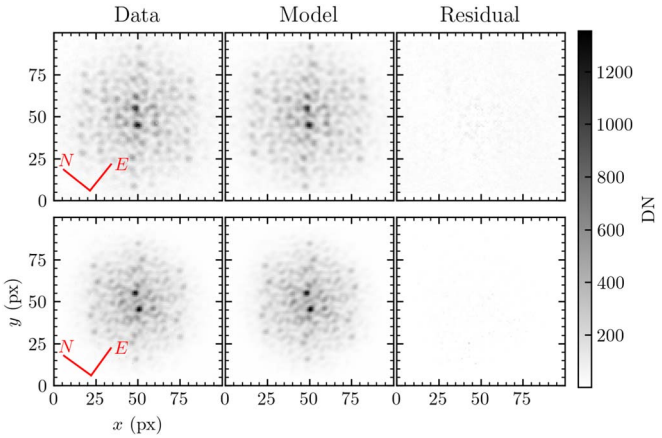

Figure 2. GPI NRM images of CD-27 (left), a model constructed from the calibrator star HD 153318 (middle), and the residual of the two (right) for the 2018 August 15 (top) and 2019 August 5 (bottom) epochs.

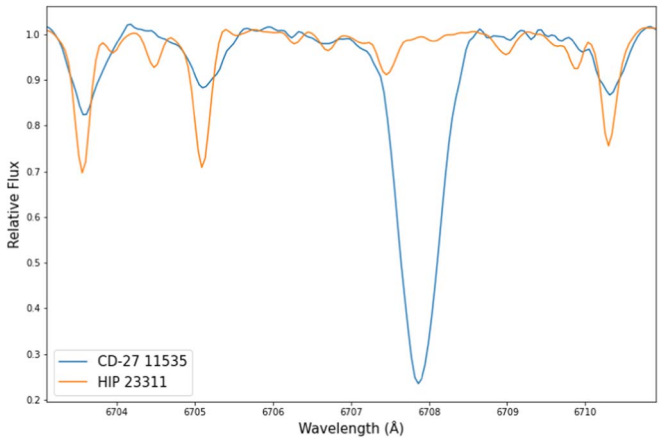

Figure 3. APO/ARCES spectra of CD-27 from 2021 June 20, showing the deep Li λ6707.79 line. Also plotted for comparison is the older K3 star HIP 23311, which has no significant lithium absorption. While the CD-27 spectrum is a composite of multiple stars of varying spectral types on the slit, the strong lithium absorption is compelling evidence for a young ($\lesssim$100 Myr) age for the system.

was corrected using a flux-conserving algorithm (Yelda et al. 2011; Service et al. 2016). The relative position and brightness of the two resolved components of the CD-27 system were calculated using the same PSF fitting approach used for both the NaCo and GPI data sets. This process was repeated for each image, yielding an average value and standard deviation for the pixel offsets and flux ratio. These were converted into on-sky separations and position angles using the calibration values listed in Table 5. The reduced images, the best-fit PSF model, and the corresponding residuals for a subset of the observations of the system are shown in Figure 1.

2.3. Gemini-S/GPI Aperture Masking

CD-27 was observed with GPI on 2018 August 15 and 2019 August 05 alongside the PSF calibrator HD 153318 (see Table 4). The GPI images were all processed and reduced with the GPI Data Reduction Pipeline (DRP) v1.5.0 (Perrin et al. 2014). After dark current subtraction and bad pixel interpolation, microspectra within the raw 2D image were extracted to create an (x, y, λ) data cube (Maire et al. 2014). An image of an argon arc lamp was taken immediately before the data to calibrate the wavelength axis of the data cube. Bad pixels were corrected using outlier rejection both before and after the data cube construction step. The system was clearly resolved into two components within the reduced image (Figure 2), at an angular separation far beyond what is typically explored with the nonredundant mask (NRM) technique. These observations were scheduled prior to a reliable determination of the orbit of the system.

Rather than using a specialized pipeline to reduce these observations (e.g., Greenbaum et al. 2019), we instead used a similar approach to that for the NaCo observations described in the previous section because of the large angular separation between the two components (Figure 2). Observations of the single calibrator star HD 153318 were reduced and used to construct a model of the PSF. Two copies of this PSF were shifted and scaled to fit the two resolved components of the CD-27 system. This process was repeated using the central wavelength slice of each observation from each epoch (19 in 2018, 16 in 2019) yielding an average and standard deviation for each measurement. On-sky separations and position angles were calculated using the relevant calibration measurements given in Table 5. The reduced images, the best-fit PSF model, and the corresponding residuals are shown in Figure 2.

2.4. APO/ARCES Spectra

We obtained optical echelle spectra of CD-27 at the Apache Point Observatory (APO) 3.5 m telescope with the ARCES instrument (Wang et al. 2003) on five epochs in 2021. Given the seeing-limited conditions and the close separation of the system, we obtained a blended spectrum of the entire system. The observations were reduced using a standard spectroscopic reduction pipeline that performs bias and flat-field correction, measures and corrects the continuum, and derives a wavelength solution from observations of a ThAr calibration lamp.

Figure 3 shows the region surrounding the Li λ6707.79 line for the CD-27 system taken on 2021 June 20 and for our RV standard HIP 23311 with a spectral type of K3 taken on the same night. Despite the near-equal visual magnitude of A and B, we do not observe double lines in our spectrum, but rather broad lines, suggesting that some or all of the components are rapid rotators. No significant RV shift is measured over our 4 months of data. We confirm the strong lithium absorption observed by Torres et al. (2006), though with these unresolved spectra we cannot determine how much lithium corresponds to each component of the system. Nevertheless, given the late spectral types of the components, with a K5 spectral type assigned to the system, this strong lithium absorption is a clear sign of youth, consistent with β Pictoris moving group membership.

3. Visual Orbit of CD –27°11535

The relative astrometry derived from our analysis and the literature astrometric measurements are compiled in Table 5. The speckle interferometry measurements from SOAR span 2016 through 2023, and we applied a correction of quadrant for consistency with our measurements.

3.1. Orbit Fitting

With the astrometry for each epoch collected, we proceed with fitting a Keplerian orbit to the relative astrometry of B

Table 2
Best-fit Orbital Parameters and Corresponding Median and 1σ Confidence Intervals for the CD-27 System

Parameter	Unit	$\chi^2_{\rm min}$ Orbit	Median, 1σ CI	Bonavita et al. (2022)
a	au	9.7	$9.8^{+0.2}_{-0.2}$	9.73 ± 0.15
e	⋯	0.2396	$0.2394^{+0.0005}_{-0.0005}$	0.264 ± 0.026
i	deg	141.39	$141.27^{+0.15}_{-0.15}$	147.2 ± 5.9
ω	deg	11.0	$11.6^{+0.5}_{-0.4}$	12.8 ± 8.8
Ω	deg	218.1	$218.4^{+0.2}_{-0.2}$	35.3 ± 4.8
T_0	yr	2029.03	$2029.06^{+0.03}_{-0.03}$	2009.35 ± 0.24
P	yr	19.81	$19.83^{+0.02}_{-0.02}$	20.78 ± 0.84
$M_{\rm tot}$	$M_\odot$	2.35	$2.36^{+0.17}_{-0.16}$	2.14 ± 0.27

Note. Values from Bonavita et al. (2022) given for comparison.

with respect to A. To do so, we use a parallel-tempered Markov Chain Monte Carlo (MCMC) procedure (Foreman-Mackey et al. 2013), implemented within the orbit fitting software orbitize! (Blunt et al. 2017). In total, 256 chains are run in parallel at 16 temperatures to sample the posterior distribution of the following eight parameters: semimajor axis (a), eccentricity (e), inclination angle (i), argument of periastron (ω), position angle of nodes (Ω), normalized epoch of periastron passage (τ), parallax (π), and total mass ($M_{\rm tot}$). Here τ is the fraction of the orbit past a given reference date (in our case 2020 January 1) and is parameterized by the period (Blunt et al. 2020).

To ensure rapid convergence of the chains, the walkers are initialized from an optimized starting position found using a rejection sampling algorithm (OFTI) to find 256 potential orbits based on the first three NaCo epochs. For the OFTI algorithm, we employ a uniform prior in total mass between 0.5 and 5 $M_\odot$. The semimajor axis prior is a log uniform distribution with a minimum value of 1×10^{-3} au and a maximum of 1×10^{7} au. Eccentricity and epoch of periastron are given uniform priors between 0.0 and 1.0. The argument of periastron and position angle of nodes also have uniform priors between 0.0 and 2π, but the inclination angle makes use of a sine prior. Finally, we use a Gaussian prior on the parallax from the parallax and error of 12.0040 ± 0.2854 mas (DR2; Gaia Collaboration et al. 2018). The priors used in the MCMC analysis were identical, other than that of the semimajor axis, which had a log uniform prior between 1×10^{-1} au and 1×10^{3} au.

Posteriors from the MCMC fit are given in Table 2, and the orbit is plotted in Figure 4 and 5. The astrometric measurements span almost a complete orbital period, resulting in a very well constrained orbit with a reduced χ^2 of 9.8. We find a fairly low eccentricity of 0.2394 ± 0.0005 and an inclination of $141.27° \pm 0.15°$. The semimajor axis of the orbit is 9.8 ± 0.2 au, with a period of 19.83 ± 0.02 yr, giving a total mass of $2.36^{+0.17}_{-0.16}$ $M_\odot$.

3.2. Comparison with Previous Studies

Recently, the CD-27 system was included in a sample of binaries characterized with VLT/SPHERE by Bonavita et al. (2022), who presented an initial determination of the orbit of this system. With our improved coverage of the orbit, we are able to further constrain the orbital parameters. Although we find similar values for the orbital period and eccentricity (see Table 2), the orbit appears rotated by 180° on the sky. This discrepancy is due to the difference between the studies for which component in the system is designated the primary. Bonavita et al. (2022) report an ambiguity in which of the two components is brightest in the near-IR, whereas we are able to differentiate which of the two resolved components is the brightest at a very high confidence ($\sim 100\sigma$ in the 2019 August 26 epoch).

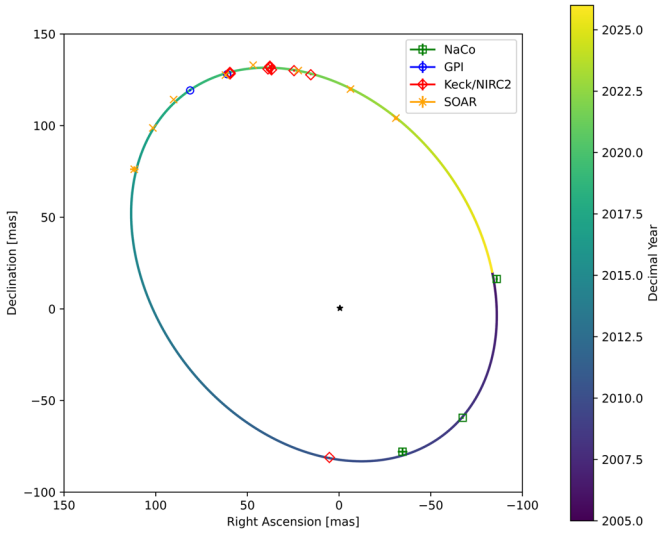

Figure 4. Best-fit visual orbit of the CD-27 system found using `orbitize!`. Different symbols and colors show the observations taken by the various instruments, while the color bar shows the relative position of the visible components over time.

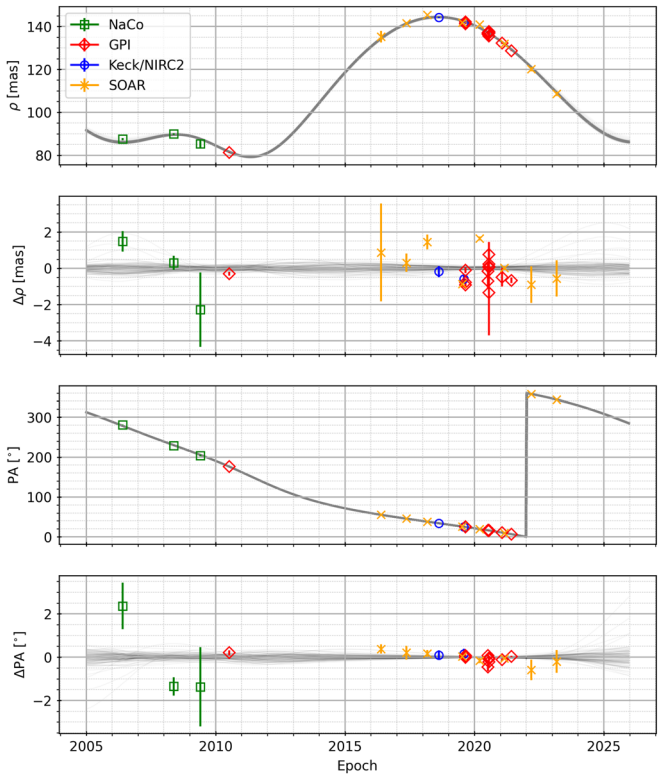

Figure 5. Astrometric measurements (symbols) and a hundred orbits randomly sampled from the MCMC posterior distributions (gray curves) showing the separation (first row) and position angle (third row) as a function of time. The second and fourth rows show the corresponding residuals relative to the median orbit.

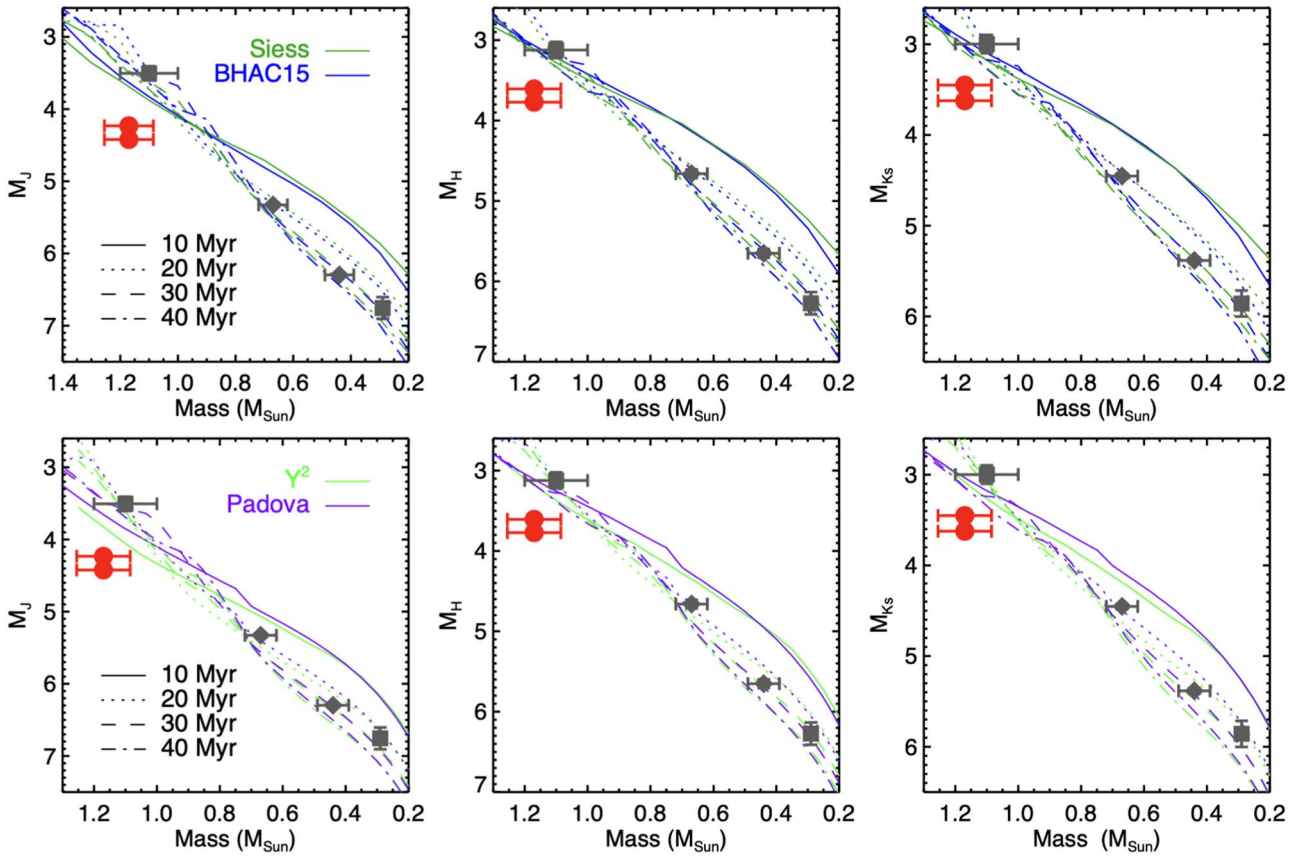

Figure 6. Comparison of the measured photometry and mass of the two resolved components of the CD-27 system (red circles) to four sets of theoretical models, as well as GJ 3305 A/B (gray diamonds) from Montet et al. (2015) and V343 Nor Aa/Ab (gray squares) from Nielsen et al. (2016). For the plotted isochrones, colors corresponds to different models, and line styles correspond to ages.

3.3. Comparison with Evolutionary Models

We compare the total system mass from the visual orbit to the masses predicted from four evolutionary model grids. As we do not have a measurement of the mass ratio of the system, we assume a mass ratio of $q = 1$, a reasonable assumption given the near-equal flux ratio. The absolute magnitude of each component was estimated from the apparent magnitude of the blended system reported in the Two Micron All Sky Survey (2MASS) catalog (Cutri et al. 2003), the flux ratio measured in the corresponding filter reported in Table 5, and the distance derived from the Gaia DR2 parallax measurement. We generated mass−magnitude relations from four evolutionary models between 10 and 40 Myr: Siess (Siess et al. 2000), BHAC15 (Baraffe et al. 2015), Yonsei−Yale (Spada et al. 2013), and Padova PARSEC (Bressan et al. 2012). These models are compared to the mass and absolute magnitudes of the two components of CD-27 in Figure 6.

Given the expected age of 26 ± 3 Myr for the system, the two components appear either underluminous or too massive when compared to the evolutionary models. Such a discrepancy is difficult to explain without invoking a systematic error in either—or both—of the component masses or absolute magnitudes. If the two stars were instead above the zero-age main sequence, that could more easily be explained by a different age of the system. This discrepancy is not sensitive to our assumed mass ratio, as changing this simply shifts the components in opposite directions horizontally relative to the model tracks. This would indeed move one of the two stars closer to the main sequence, but the other would become an even greater outlier.

4. Possible Causes of the Discrepancy

4.1. An Additional Component

A low-mass third companion to either of the two resolved components of the system could explain the discrepancy between the total mass from the orbit and the mass predicted from the absolute magnitude of each component. We test this hypothesis by simultaneously fitting the visual orbit and the spectral energy distribution of both of the resolved components under various assumptions regarding the system architecture. Specifically, we investigate a binary (AB) and a triple with the additional companion around either the primary (AaAb-B) or the secondary (A-BaBb). We also test the effect of removing the Gaia DR2 parallax constraint on the quality of the fit. We use Metropolis−Hastings MCMC implemented within the `emcee` package (Foreman-Mackey et al. 2013) to simultaneously fit the visual orbit, the flux ratios between the two resolved components, and the total near-infrared flux of the system. The visual orbit is fit as before (Section 3). The flux ratios and total flux of the system are estimated from the four aforementioned evolutionary models, with an independent fit performed per model grid. Due to the 2.9-day variability of the system (Kiraga 2012), we only use flux ratio measurements taken on 2020 July 24 that were taken in five different bands within an hour and, consequently, would be less affected by variability. For each fit, we run 128 chains in parallel for 10^4

Table 3
Possible Configurations of CD-27

Configuration	Prior on Parallax	Evolutionary Model	Min χ^2	Age (Myr)	Parallax (mas)	M_1 ($M_\odot$)	M_2 ($M_\odot$)	M_3 ($M_\odot$)
AaAb-B	Flat	BHAC15	2.8	$23.6^{+1.9}_{-1.9}$	$12.72^{+0.11}_{-0.13}$	$0.906^{+0.006}_{-0.007}$	$0.881^{+0.009}_{-0.008}$	$0.171^{+0.056}_{-0.046}$
		Padova	2.8	$22.8^{+1.8}_{-1.8}$	$12.66^{+0.11}_{-0.12}$	$0.916^{+0.008}_{-0.008}$	$0.888^{+0.008}_{-0.008}$	$0.181^{+0.051}_{-0.046}$
		Seiss	5.9	$24.5^{+1.8}_{-1.8}$	$12.41^{+0.10}_{-0.13}$	$0.984^{+0.009}_{-0.010}$	$0.955^{+0.009}_{-0.009}$	$0.169^{+0.062}_{-0.047}$
		Yonsei−Yale	6.3	$25.9^{+2.0}_{-1.9}$	$12.69^{+0.16}_{-0.20}$	$0.905^{+0.009}_{-0.011}$	$0.875^{+0.016}_{-0.019}$	$0.193^{+0.083}_{-0.062}$
	Gaia DR2	BHAC15	2.7	$23.4^{+1.8}_{-1.8}$	$12.59^{+0.12}_{-0.11}$	$0.907^{+0.006}_{-0.007}$	$0.888^{+0.008}_{-0.009}$	$0.222^{+0.051}_{-0.051}$
		Padova	2.7	$22.8^{+1.7}_{-1.7}$	$12.57^{+0.11}_{-0.10}$	$0.916^{+0.008}_{-0.007}$	$0.893^{+0.008}_{-0.008}$	$0.218^{+0.047}_{-0.047}$
		Seiss	5.5	$24.4^{+1.7}_{-1.8}$	$12.34^{+0.12}_{-0.13}$	$0.984^{+0.009}_{-0.010}$	$0.958^{+0.009}_{-0.009}$	$0.200^{+0.061}_{-0.057}$
		Yonsei−Yale	6.6	$25.4^{+1.9}_{-1.8}$	$12.48^{+0.15}_{-0.12}$	$0.906^{+0.008}_{-0.010}$	$0.888^{+0.011}_{-0.014}$	$0.276^{+0.056}_{-0.065}$
A-B	Flat	BHAC15	5.8	$23.7^{+1.8}_{-1.7}$	$13.16^{+0.04}_{-0.04}$	$0.904^{+0.006}_{-0.007}$	$0.862^{+0.006}_{-0.006}$	⋯
		Padova	5.1	$22.2^{+2.0}_{-2.0}$	$13.13^{+0.04}_{-0.04}$	$0.915^{+0.008}_{-0.008}$	$0.866^{+0.007}_{-0.007}$	⋯
		Seiss	5.9	$24.1^{+1.7}_{-1.7}$	$12.79^{+0.04}_{-0.04}$	$0.984^{+0.009}_{-0.009}$	$0.939^{+0.007}_{-0.007}$	⋯
		Yonsei−Yale	6.9	$26.7^{+1.8}_{-1.9}$	$13.24^{+0.06}_{-0.07}$	$0.897^{+0.011}_{-0.012}$	$0.840^{+0.015}_{-0.011}$	⋯
	Gaia DR2	BHAC15	5.5	$23.2^{+1.7}_{-1.7}$	$13.14^{+0.04}_{-0.03}$	$0.907^{+0.006}_{-0.006}$	$0.865^{+0.006}_{-0.006}$	⋯
		Padova	5.2	$21.9^{+1.8}_{-1.9}$	$13.10^{+0.04}_{-0.04}$	$0.918^{+0.008}_{-0.008}$	$0.870^{+0.007}_{-0.007}$	⋯
		Seiss	5.9	$23.8^{+1.6}_{-1.6}$	$12.78^{+0.04}_{-0.04}$	$0.987^{+0.008}_{-0.009}$	$0.941^{+0.007}_{-0.007}$	⋯
		Yonsei−Yale	7.2	$25.4^{+1.8}_{-1.8}$	$13.17^{+0.06}_{-0.06}$	$0.907^{+0.009}_{-0.011}$	$0.853^{+0.014}_{-0.014}$	⋯
A-BaBb	Flat	BHAC15	10.6	$22.9^{+1.7}_{-1.7}$	$12.86^{+0.04}_{-0.05}$	$0.916^{+0.007}_{-0.006}$	$0.861^{+0.006}_{-0.006}$	$0.113^{+0.020}_{-0.010}$
		Padova	11.8	$20.3^{+2.4}_{-2.1}$	$12.84^{+0.04}_{-0.05}$	$0.929^{+0.008}_{-0.007}$	$0.865^{+0.008}_{-0.008}$	$0.108^{+0.013}_{-0.006}$
		Seiss	10.9	$23.6^{+1.6}_{-1.6}$	$12.51^{+0.05}_{-0.06}$	$0.998^{+0.008}_{-0.008}$	$0.940^{+0.006}_{-0.006}$	$0.119^{+0.028}_{-0.014}$
		Yonsei−Yale	10.6	$26.0^{+1.7}_{-1.7}$	$12.84^{+0.08}_{-0.11}$	$0.920^{+0.009}_{-0.010}$	$0.847^{+0.013}_{-0.011}$	$0.132^{+0.047}_{-0.024}$
	Gaia DR2	BHAC15	12.4	$22.7^{+1.7}_{-1.7}$	$12.83^{+0.05}_{-0.07}$	$0.918^{+0.007}_{-0.006}$	$0.862^{+0.006}_{-0.006}$	$0.121^{+0.028}_{-0.015}$
		Padova	11.3	$20.2^{+2.3}_{-2.0}$	$12.82^{+0.04}_{-0.05}$	$0.932^{+0.008}_{-0.007}$	$0.867^{+0.008}_{-0.008}$	$0.111^{+0.018}_{-0.008}$
		Seiss	9.6	$23.4^{+1.6}_{-1.7}$	$12.49^{+0.05}_{-0.07}$	$1.000^{+0.008}_{-0.008}$	$0.941^{+0.006}_{-0.006}$	$0.125^{+0.034}_{-0.019}$
		Yonsei−Yale	12.0	$25.5^{+1.6}_{-1.6}$	$12.71^{+0.13}_{-0.16}$	$0.928^{+0.010}_{-0.010}$	$0.849^{+0.013}_{-0.011}$	$0.183^{+0.071}_{-0.054}$

Note. M_1 is A or Aa, M_2 refers to B or Ba, while M_3 is the mass of Ab or Bb.

steps. The walkers are initialized with uniform distributions, centered at the values reported in Section 3. At each step in the fit, the flux of each constituent star is generated using an interpolating function given its age, mass, and the evolutionary model, from which the flux ratio between the two resolved components is determined. The absolute magnitude of the blended system is calculated and converted into an apparent magnitude using the parallax, which is then compared to the 2MASS measurements for the system (Cutri et al. 2003). We use priors to keep the age between 10 and 100 Myr (consistent with the amount of lithium absorption observed), the parallax positive, and the mass of the constituent stars between 0.1 and 1.5 $M_\odot$. The priors on the orbital parameters are as used in Section 3. The lower bound on the star mass prior was set by the minimum mass reported in the evolutionary models.

The results of our experiment are reported in Table 3. A representative example of the model fluxes (in an AaAb-B configuration), their flux ratio and our data points is included in Figure 7. We find a best fit to the BHAC15 and Padova model grids in the AaAb-B configurations, with a minimum χ^2 of 2.8, excluding the contribution from the visual orbit fit, compared with ∼5 for the A-B configuration and 10–12 for the A-BaBb configuration. The Seiss and Yonsei−Yale models show similar goodness of fit for the A-B and AaAb-B configurations, with the A-BaBb configuration being more strongly disfavored. The fits with and without a prior on the parallax give a generally similar goodness of fit, due in part to the relatively large uncertainty of the Gaia DR2 parallax measurement. This joint fit of the astrometric and photometric measurements of the CD-27 system provides some evidence of an unresolved companion to the A component within the CD-27 system,

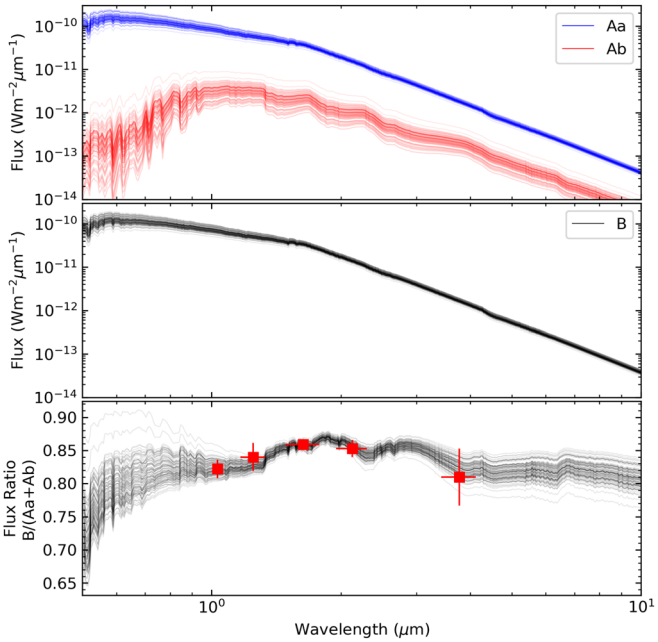

Figure 7. Model fluxes of stars Aa and Ab (top panel) and B (middle panel), and the flux ratio of the resolved pair AaAb and B (bottom panel) as a function of wavelength from the Padova evolutionary model for 100 samples drawn from our MCMC analysis. The red squares represent the flux ratio between the two components measured in the Keck/NIRC2 images taken on 2020 July 24.

although the improvement in the goodness of fit does depend on which evolutionary model is used. We compute the component masses for the AaAb-B system architecture by

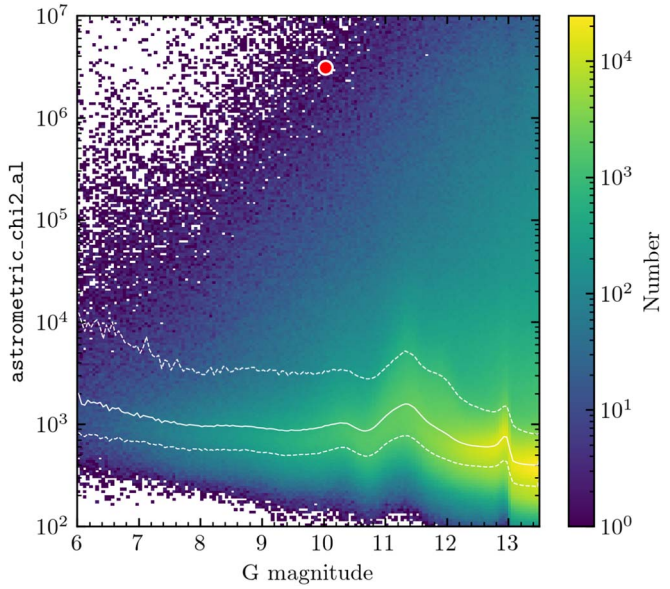

Figure 8. The χ^2 reported in the Gaia DR3 catalog for the fit to the astrometric measurements of CD-27 (red point) compared to stars of a range of magnitudes. CD-27 has a χ^2 larger than 99.5% of stars within 0.1 mag. This is consistent with the variability of CD-27 biasing the Gaia DR2 5-parameter fit, casting doubt on the accuracy of the parallax.

taking the weighted average of the four model-dependent results and find $M_{\rm Aa} = 0.923 \pm 0.008\ M_\odot$, $M_{\rm Ab} = 0.177 \pm 0.055\ M_\odot$, and $M_{\rm B} = 0.903 \pm 0.009\ M_\odot$. The age of the system with this method is 24.1 ± 1.9 Myr, and the parallax is 12.61 ± 0.13 mas.

4.2. An Overestimated Distance

Estimating the system mass and absolute magnitudes of both components requires a reliable measurement of the system parallax. The discrepancy between measured and predicted system mass could be explained by decreasing the distance to the star. This would cause a decrease in the system mass due to a decrease in the semimajor axis, and it would decrease the absolute magnitudes of the two components. This scenario was considered in Section 4.1, where we found no significant difference in the goodness of fit when comparing fits where the parallax was constrained based on the Gaia DR2 measurement to those where it was allowed to float freely. Nevertheless, the large uncertainty on the parallax measurement suggests that this is a plausible explanation for the observed discrepancy.

The astrometric parameters of the CD-27 system reported in Gaia DR2 are derived from a five-parameter astrometric fit (position, proper motion, parallax) based on 111 measurements taken over the course of almost 2 yr. All of the sources within Gaia DR2 were treated as single stars, assuming constant linear motion over the time span of the mission. Stars that deviate from linear motion for whatever reason will still be fit using the same five-parameter model, but the goodness of fit will suffer owing to the incorrect assumption of linear motion. For CD-27, Gaia DR2 reports a unit weight error of $u = 4.8$, well above the typical value of $u = 1.4$ for stars with $G \sim 10$ (Gaia Collaboration et al. 2018). This poor goodness of fit is reflected in the unusually large uncertainties on the five fitted astrometric parameters. The goodness of fit is significantly worse in the subsequent Gaia Data Release 3 (DR3; Gaia Collaboration et al. 2021), as shown in Figure 8, and only a two-parameter solution was presented. The star was not listed in the nonsingle star supplement in DR3, suggesting that an astrometric binary solution was attempted but rejected.

We consider two plausible causes for this apparent deviation from linear motion that could explain the poor goodness of fit in both Gaia DR2 and DR3 and that could have biased the parallax measurement reported in Gaia DR2. We first consider the effect of orbital motion of the two known components over the course of the Gaia observations. We use the orbit fit presented in Section 3 and the flux ratios in Table 5, under the assumption that $\Delta G \sim \Delta z$, to predict the motion of the photocenter as observed by Gaia from 2014 July 25 to 2016 May 23. We predict almost linear motion in the decl. direction with little change in R.A. This would manifest itself as a small change to the measured proper motion of the system rather than inducing significant nonlinear motion. It is unlikely that the orbital motion of the two resolved components could explain the poor goodness of fit in Gaia DR2.

Another source of nonlinear astrometric motion in long-period binary systems is the variability of one or both of the components. So-called variability-induced movers (VIMs; Wielen 1996) are systems in which the periodic variability of an unresolved binary causes the photocenter to move in a characteristic fashion. Several examples have been identified in the Hipparcos and Gaia DR3 catalogs. Using the measured $\sim$15% amplitude of the V-band variability of this system (Kiraga 2012), we estimate that the variability can shift the Gaia photocenter relative to the barycenter by as much as 10 mas between minima and maxima if the variability is confined to one component. Given that this is comparable to the amplitude of the parallax signal, it is likely that significant variability could significantly bias the parallax measurements. Unfortunately, without access to the individual Gaia measurements, it is not possible to attempt to fit the parallax while simultaneously modeling this effect. CD-27 is not flagged as a VIM in Gaia DR3, and it is not possible to ascertain whether such a solution was attempted.

5. Limits on the Presence of Additional Companions

5.1. Lower Limit from Spectroscopy

Our spectroscopic measurements can be used to place a lower limit on the orbital period of an additional companion within the system. A low-mass companion on a very short orbital period would induce a significant change of the RV of the star it orbits, so long as the orbit is not face-on. We search for the effects of a third component within the ARCES spectra by cross-correlating each with the spectrum of HIP 41277, a K8 star with a comparable $v \sin i$ to CD-27. We use eight orders of the ARCES spectrum covering $\sim$5500−6700 Å, each with several lines and high S/N. The resulting cross-correlation function has a single peak for each epoch, and we do not measure a significant variation of the RV. To explore the effects of relative RV and rotational broadening on the cross-correlation function, we generate a synthetic binary spectrum with varying RV offsets and rotational velocities that we cross-correlate with the spectrum of HIP 41277. We generate the simulated binary by combining two copies of a spectrum of a K5 star we observed as an RV standard (HIP 48331; Soubiran et al. 2013). Each spectrum is rotationally broadened and scaled based on the predicted optical flux ratio for the two stars. We sum and normalize the blended spectrum, which is then cross-

correlated with HIP 41277. This process is repeated for a grid of RV offsets (six between 0 and 40 km s^{-1}) and $v \sin i$ (four between 5 and 20 km s^{-1}). The resulting cross-correlation functions are shown in Figure 12. At small delta RV ($\lesssim$25 km s^{-1}) and $v \sin i$ ($\lesssim$5 km s^{-1}), the cross-correlation function has a single peak. When lines are broadened by rotation ($v \sin i \gtrsim 20$ km s^{-1}), a larger delta RV ($\gtrsim$40 km s^{-1}) is required to resolve them. We identify the delta RV at which we detect two visually distinct peaks in the cross-correlation function, indicating a detectable separation between the primary and secondary absorption lines. Typical $v \sin i$ for K-type stars in the β Pic moving group are 10−13 km s^{-1} (Zuckerman et al. 2001). For $v \sin i = 10$ km s^{-1}, the smallest delta RV at which we see two distinct peaks is ∼25 km s^{-1}. For $v \sin i = 13$ km s^{-1}, the smallest delta RV at which we see two distinct peaks is ∼30 km s^{-1}. The predicted delta RV from our orbit fit for A and B alone is ∼5 km s^{-1}. Thus, there can be an additional delta RV $\gtrsim$25 km s^{-1} caused by the orbit of a companion around either component that would remain undetectable in our ARCES spectra. This upper limit on the RV, assuming zero eccentricity, a 90° inclination angle, and the masses given in row 2 of Table 3, corresponds to a semimajor axis larger than 0.04 au (orbital period >0.01 yr).

5.2. Upper Limit from Astrometry

As there is no obvious Keplerian signal in the residuals of the orbit fit to our astrometric measurements (Figure 5, second and fourth panels), we can place an upper limit on the semimajor axis of an inner binary. We make the conservative assumption that an orbit with a photocenter semiamplitude of 2 mas in the near-infrared would have easily been detected. Using the predicted masses and fluxes of the three components given for the AaAb-B configuration in Table 3, we convert this maximum photocenter semimajor axis into an upper limit on the total semimajor axis of the inner subsystem. We compute the reduced mass $B = M_2/(M_1 + M_2)$ and reduced flux $\beta = F_2/(F_1 + F_2)$, from which we can calculate the total semimajor axis as $a = a_p/(B - \beta)$. We find a conservative upper limit for the semimajor axis of the inner binary of ∼1.6 au (orbital period <2.0 yr). The allowed phase space for the semimajor axis of an inner binary is shown in Figure 9.

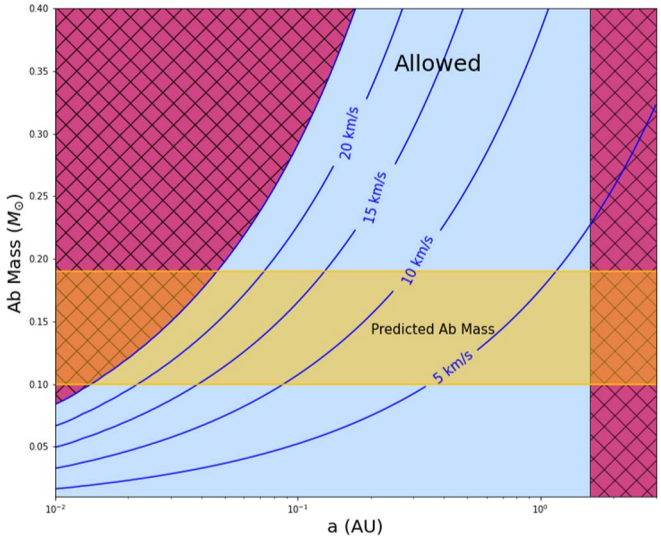

Figure 9. The pink hatched regions indicate mass−separation combinations that are not allowed for Ab. On the left, the semimajor axis is limited by the maximum possible RV (∼25 km s^{-1}) of Aa induced by Ab over a range of Ab masses. The range of predicted Ab masses is highlighted in yellow. On the right, the lack of a detectable wobble in the astrometric measurements allows us to draw a conservative upper limit of ∼1.6 au for the subsystem semimajor axis from the largest separation residual (∼2 mas) and dynamical arguments.

6. Conclusion

We have presented resolved astrometric measurements of the young CD-27 system that we used to refine the visual orbit of the system. Our analysis revealed a significant discrepancy between the total system mass and the masses of the components estimated for evolutionary models. We explored two scenarios that could explain this discrepancy: either an unresolved companion to either of the two stars, or a biased parallax measurement caused by the photometric variability of either or both of the components. Our joint fit of the visual orbit and resolved photometry provides evidence for a low-mass star present around the A component of the system. Our most favored configuration for this scenario is a K-type star and M dwarf in a short but unknown orbit (with a semimajor axis between 0.04 and 1.6 au), with a more distant K-type star in a ∼20 yr orbit with a semimajor axis of 9.8 au. This configuration is favored for the BHAC15 and Padova model grids regardless of whether the parallax is constrained using the Gaia DR2 measurement or not.

An alternative explanation for the observed discrepancy between the measured and predicted system mass is a bias in the parallax measurement reported in Gaia DR2. CD-27 has a very poor goodness of fit in both Gaia DR2 and DR3, so much so that only a two-parameter fit is provided in the DR3. We exclude the possibility that this poor goodness of fit is caused by the photocenter orbit of the known binary; the orbital motion is almost linear over the Gaia baseline. Instead, it is likely that the photometric variability of one or both of the components is causing a significant motion of the photocenter relative to the barycenter on periods comparable to the 2.9-day variability measured by Kiraga (2012). The amplitude of this variability-induced motion is predicted to be on the same order as the amplitude of the parallax signal. Unfortunately, without the individual Gaia measurements, it is impossible to refit the parallax accounting for this effect.

Currently, the uncertainty regarding the architecture of the system is primarily driven by uncertainty in the parallax. The upcoming Gaia data releases will contain the individual astrometric measurements made during the 5 and 10 yr durations of the mission, covering a good fraction of the orbital period of the system. With these data in hand, we will be able to jointly fit the systemic motion and parallax of the system, the orbital motion, and motion induced by variability of either or both of the resolved components. With a refined distance estimate in hand, we will be able to revisit the observed discrepancy between the measured and predicted system mass. In the mean time, interferometric observations from CHARA (ten Brummelaar et al. 2005) and VLTI (Correia et al. 2003), as well as high-resolution near-infrared spectroscopic observations, will be able to place improved constraints on the presence of additional companions, complementing the analysis performed here. A complete characterization of the CD-27 system, in terms of both an improved distance determination and a more detailed search for additional companion, will be necessary before the system can be used

as a valuable benchmark for the study of the evolution of young stars.

Acknowledgments

This work was supported in part by NASA grants NNX14AJ80G, 80NSSC21K0958 (E.L.N. and A.E.P.), and 21-ADAP21-0130 (E.L.N. and A.S.) and authored by employees of Caltech/IPAC under contract No. 80GSFC21R0032 with the National Aeronautics and Space Administration. Some of the data presented herein were obtained at the W. M. Keck Observatory, which is operated as a scientific partnership among the California Institute of Technology, the University of California, and the National Aeronautics and Space Administration. The Observatory was made possible by the generous financial support of the W. M. Keck Foundation. The authors wish to recognize and acknowledge the very significant cultural role and reverence that the summit of Maunakea has always had within the indigenous Hawaiian community. We are most fortunate to have the opportunity to conduct observations from this mountain. This work is partially based on observations obtained at the international Gemini Observatory, a program of NSF's NOIRLab, which is managed by the Association of Universities for Research in Astronomy (AURA) under a cooperative agreement with the National Science Foundation on behalf of the Gemini Observatory partnership: the National Science Foundation (United States), National Research Council (Canada), Agencia Nacional de Investigación y Desarrollo (Chile), Ministerio de Ciencia, Tecnología e Innovación (Argentina), Ministério da Ciência, Tecnologia, Inovações e Comunicações (Brazil), and Korea Astronomy and Space Science Institute (Republic of Korea). This research has also made use of the VizieR catalog access tool, CDS, Strasbourg, France (DOI :10.26093/cds/vizier) and the SIMBAD database, operated at the same location. The original description of the VizieR service was published in 2000, A&AS 143, 23. Further, this work presents results from the European Space Agency (ESA) space mission Gaia. Gaia data are being processed by the Gaia Data Processing and Analysis Consortium (DPAC). Funding for the DPAC is provided by national institutions, in particular the institutions participating in the Gaia MultiLateral Agreement (MLA). The Gaia mission website is https://www.cosmos.esa.int/gaia. The Gaia archive website is https://archives.esac.esa.int/gaia. Finally, this publication makes use of data products from the Two Micron All Sky Survey, which is a joint project of the University of Massachusetts and the Infrared Processing and Analysis Center/California Institute of Technology, funded by the National Aeronautics and Space Administration and the National Science Foundation.

Appendix

Table 4 presents the observing log of all epochs for CD-27 and calibrators for which we reduced data. Table 5 contains all astrometric and photometric measurements of the star—both our own and those found in the literature—as well as the residuals compared to the median orbit. Figure 10 shows the corner plot of the orbital parameters from the initial `orbitize!` fit and reveals convergence. Figure 11 displays the covariance between the system age, parallax, and component masses from the joint fit in Section 4 using the evolutionary model and system architecture with the lowest χ^2—AaAb-B and Padova PARSEC. Figure 12 shows the cross-correlation function between one observed spectrum of CD-27 and HIP 41277, as well as a simulated binary and HIP 41277 for various $v \sin i$ and ΔRV.

Table 4
Observing Log of CD-27 and Suitable PSF Calibrators

UT Start	Target	Camera	Filter	$t_{\rm dit}$ (s)	$n_{\rm dit}$	$n_{\rm exp}$	DIMM Seeing (arcsec)	Air Mass	Program ID
			VLT/NaCo						
2006-05-27T04:40:28	CD –27°11535	S27	IB2.27	1.2	50	12	0.99–1.34	1.01–1.03	077.C-0483
2006-05-27T01:23:21	1RXS J125608.8–692652	S27	IB2.27	50	1.2	16	1.19–1.62	1.41	077.C-0483
2006-05-27T02:00:28	HD 112245	S27	IB2.27	75	0.8	13	1.08–1.95	1.26–1.27	077.C-0483
2006-05-27T06:57:01	CD –54°7336	S27	IB2.27	75	0.8	12	0.93–1.32	1.18–1.20	077.C-0483
2008-05-18T04:17:54	CD –27°11535	S27	IB2.27	60	1.0	12	0.67–1.23	1.08–1.11	081.C-0825
2008-05-19T06:22:59	GSC 06242–00004	S27	IB2.27	150	0.4	12	0.70–0.92	1.00–1.01	081.C-0825
2008-05-19T05:57:49	TYC 6234-1287-1	S27	IB2.27	40	1.5	12	0.59–0.72	1.01	081.C-0825
2008-05-17T03:27:16	CD –25°11504	S27	IB2.27	100	0.6	12	0.65–0.81	1.09–1.12	081.C-0825
2008-05-17T03:50:14	V* V2505 Oph	S27	IB2.27	120	0.5	12	0.59–0.67	1.07–1.09	081.C-0825
2009-06-01T06:13:30	CD –27°11535	S13	$K_{\rm s}$/ND	5	2	9	1.32–1.84	1.03	083.C-0659
2009-06-01T00:27:49	2MASS J12205449 –6457242	S13	$K_{\rm s}$/ND	5	2	6	0.58–0.74	1.31–1.34	083.C-0659
2009-06-01T02:08:17	CD –40°8031	S13	$K_{\rm s}$/ND	5	2	3	0.90	1.05	083.C-0659
2009-06-01T03:24:20	V* NZ Lup	S13	$K_{\rm s}$/ND	5	2	3	0.78	1.06	083.C-0659
			Keck/NIRC2						
2010-07-12T08:59:21	CD –27°11535	Narrow	$K_{\rm s}$	0.100	100	6		1.51–1.52	U104N2
2010-07-12T09:58:40	HD 172649	Narrow	$K_{\rm s}$	0.032	100	6		1.05–1.06	U104N2
2019-08-26T05:14:34	CD –27°11535	Narrow	K'	0.050	100	22		1.48	U204
2019-08-26T05:20:45	CD –27°11535	Narrow	H	0.050	100	22		1.48	U204
2019-08-26T05:28:22	CD –27°11535	Narrow	J	0.050	100	42		1.48	U204
2019-08-26T05:53:51	HD 160934	Narrow	K'	0.018	100	42		1.33	U204
2019-08-26T05:53:51	HD 160934	Narrow	H	0.018	100	42		1.33	U204
2019-08-26T06:06:23	HD 160934	Narrow	J	0.018	100	42		1.33–1.34	U204
2020-07-09T07:16:01	CD –27°11535	Narrow	H	0.05	100	41		1.56–1.58	D309
2020-07-09T07:26:26	CD –27°11535	Narrow	z	0.60	10	41		1.53–1.55	D309
2020-07-09T07:56:21	HD 153318	Narrow	z	0.60	10	42		1.60	D309
2020-07-09T08:19:32	HD 153318	Narrow	H	0.05	100	41		1.60	D309
2020-07-24T06:46:54	CD –27°11535	Narrow	H	0.05	100	25		1.51	U216
2020-07-24T06:53:56	CD –27°11535	Narrow	J	0.05	100	25		1.50	U216
2020-07-24T07:00:53	CD –27°11535	Narrow	K'	0.05	100	25		1.49–1.50	U216
2020-07-24T07:09:30	CD –27°11535	Narrow	z	2.00	4	25		1.48–1.49	U216
2020-07-24T07:16:52	CD –27°11535	Narrow	L'	0.30	10	25		1.48	U216
2020-07-24T07:25:54	HD 153318	Narrow	L'	0.30	10	50		1.60–1.61	U216
2020-07-24T07:39:45	HD 153318	Narrow	z	2.00	4	25		1.61–1.62	U216
2020-07-24T07:47:25	HD 153318	Narrow	K'	0.05	100	25		1.62–1.63	U216
2020-07-24T07:53:55	HD 153318	Narrow	J	0.05	100	25		1.63–1.64	U216
2020-07-24T08:00:26	HD 153318	Narrow	H	0.05	100	15		1.64–1.65	U216
2021-01-23T16:25:29	CD –27°11535	Narrow	K'	0.3	50	15		2.51–2.62	D297
2021-01-23T16:16:42	HD 153318	Narrow	K'	0.1	100	20		2.45–2.38	D297
2021-06-04T11:33:58	CD –27°11535	Narrow	BrG	0.3	100	12		1.52–1.54	D335
2021-06-04T12:22:24	1RXS J195602.8 –320720	Narrow	BrG	1.0	30	12		1.68–1.70	D335
			Gemini-S/GPI						
2018-08-15T01:05:15	CD –27°11535	⋯	H	59.6	1	19		1.01–1.03	GS-2017B-Q-22
2018-08-15T01:46:28	HD 153318	⋯	H	59.6	1	20		1.07–1.11	GS-2017B-Q-22
2019-08-05T02:14:09	CD –27°11535	⋯	K_1	59.6	1	16		1.04–1.06	GS-2019B-Q-120
2019-08-05T02:41:50	HD 153318	⋯	K_1	59.6	1	16		1.09–1.13	GS-2019B-Q-120

Table 5
Astrometric and Photometric Measurements of CD-27

UT Date	Instrument	Filter	Plate Scale (mas pixel^{-1})	True North (deg)	ρ (mas)	ρ Residual (mas)	θ (deg)	θ Residual (deg)	Flux Ratio	Calib. Reference	Data Reference
2006 May 27	NaCo	IB2.27	27.06 ± 0.06	0.02 ± 0.1	88.45 ± 0.78	1.48	282 ± 2	2.37	0.87 ± 0.05	1	
2008 May 18	NaCo	IB2.27	27.08 ± 0.03	0.04 ± 0.09	91.85 ± 0.46	0.30	229.4 ± 0.4	−1.35	0.841 ± 0.014	1	
2009 Jun 01	NaCo	K_s/ND	13.22 ± 0.02	-0.17 ± 0.03	83.26 ± 3.37	−2.29	203 ± 2	−1.37	0.880 ± 0.023	2	
2010 Jul 12	NIRC2	K_s	9.952 ± 0.002	0.252 ± 0.009	81.28 ± 0.11	−0.30	176.30 ± 0.11	0.21	0.805 ± 0.007	3	
2018 Aug 15	GPI	H	14.161 ± 0.021	0.28 ± 0.19	144.23 ± 0.31	−0.19	34.26 ± 0.22	0.09	⋯	4	
2019 Aug 05	GPI	K_1	14.161 ± 0.021	0.45 ± 0.11	141.85 ± 0.23	−0.59	25.47 ± 0.23	0.16	⋯	4	
2019 Aug 26	NIRC2	J	9.971 ± 0.005	-0.26 ± 0.02	141.42 ± 0.14	−0.11	24.82 ± 0.05	−0.02	0.863 ± 0.006	5	
2019 Aug 26	NIRC2	H	9.971 ± 0.005	-0.26 ± 0.02	141.28 ± 0.14	−0.93	24.86 ± 0.04	0.08	0.884 ± 0.003	5	
2019 Aug 26	NIRC2	K'	9.971 ± 0.005	-0.26 ± 0.02	142.10 ± 0.16	−0.79	24.76 ± 0.04	0.04	0.873 ± 0.002	5	
2020 Jul 09	NIRC2	H	9.971 ± 0.005	-0.26 ± 0.02	136.5 ± 0.4	−0.71	16.48 ± 0.05	0.08	0.871 ± 0.008	5	
2020 Jul 09	NIRC2	z	9.971 ± 0.005	-0.26 ± 0.02	137.0 ± 0.4	−0.16	15.94 ± 0.18	−0.46	0.857 ± 0.013	5	
2020 Jul 24	NIRC2	H	9.971 ± 0.005	-0.26 ± 0.02	136.9 ± 0.2	0.04	15.94 ± 0.06	−0.05	0.859 ± 0.005	5	
2020 Jul 24	NIRC2	J	9.971 ± 0.005	-0.26 ± 0.02	137.1 ± 0.9	0.22	15.9 ± 0.1	−0.08	0.84 ± 0.02	5	
2020 Jul 24	NIRC2	K'	9.971 ± 0.005	-0.26 ± 0.02	137.7 ± 0.7	0.76	15.90 ± 0.07	−0.09	0.853 ± 0.013	5	
2020 Jul 24	NIRC2	z	9.971 ± 0.005	-0.26 ± 0.02	137.0 ± 0.9	0.10	15.95 ± 0.08	−0.04	0.822 ± 0.014	5	
2020 Jul 24	NIRC2	L'	9.971 ± 0.005	-0.26 ± 0.02	136 ± 2	−1.35	15.8 ± 0.3	−0.22	0.81 ± 0.04	5	
2021 Jan 22	NIRC2	K'	9.971 ± 0.005	-0.26 ± 0.02	131.5 ± 0.9	−0.49	10.77 ± 0.13	−0.11	0.92 ± 0.02	5	
2021 Jun 04	NIRC2	BrG	9.971 ± 0.005	-0.26 ± 0.02	128.68 ± 0.15	−0.67	6.88 ± 0.03	0.03	0.887 ± 0.005	5	
Literature Measurements											
2016 May 20	SOAR	I			135.2 ± 2.7	0.87	55.7 ± 0.2	0.38			6
2017 May 15	SOAR	I			141.6 ± 0.5	0.30	45.8 ± 0.3	0.20			6
2018 Mar 07	SOAR	I			145.5 ± 0.4	1.44	38.3 ± 0.2	0.17			7
2019 Jul 15	SOAR	I			141.8 ± 0.2	−0.87	25.9 ± 0.1	0.03			8
2020 Mar 13	SOAR	I			141.0 ± 0.1	1.64	19.4 ± 0.08	−0.16			9
2021 Feb 27	SOAR	I			131.9 ± 0.1	0.01	9.7 ± 0.04	−0.06			10
2022 Mar 12	SOAR	I			120.1 ± 1.0	−0.90	357.01 ± 0.48	−0.56			11
2023 Mar 06	SOAR	I			108.6 ± 1.0	−0.56	343.41 ± 0.53	−0.20			11

References: (1) Ehrenreich et al. (2010); (2) Chauvin et al. (2015); (3) Yelda et al. (2011); (4) De Rosa et al. (2020); (5) Service et al. (2016); (6) Tokovinin et al. (2018); (7) Tokovinin et al. (2019); (8) Tokovinin et al. (2020); (9) Tokovinin et al. (2021); (10) Tokovinin et al. (2022); (11) A. Tokovinin (2023, private communication).

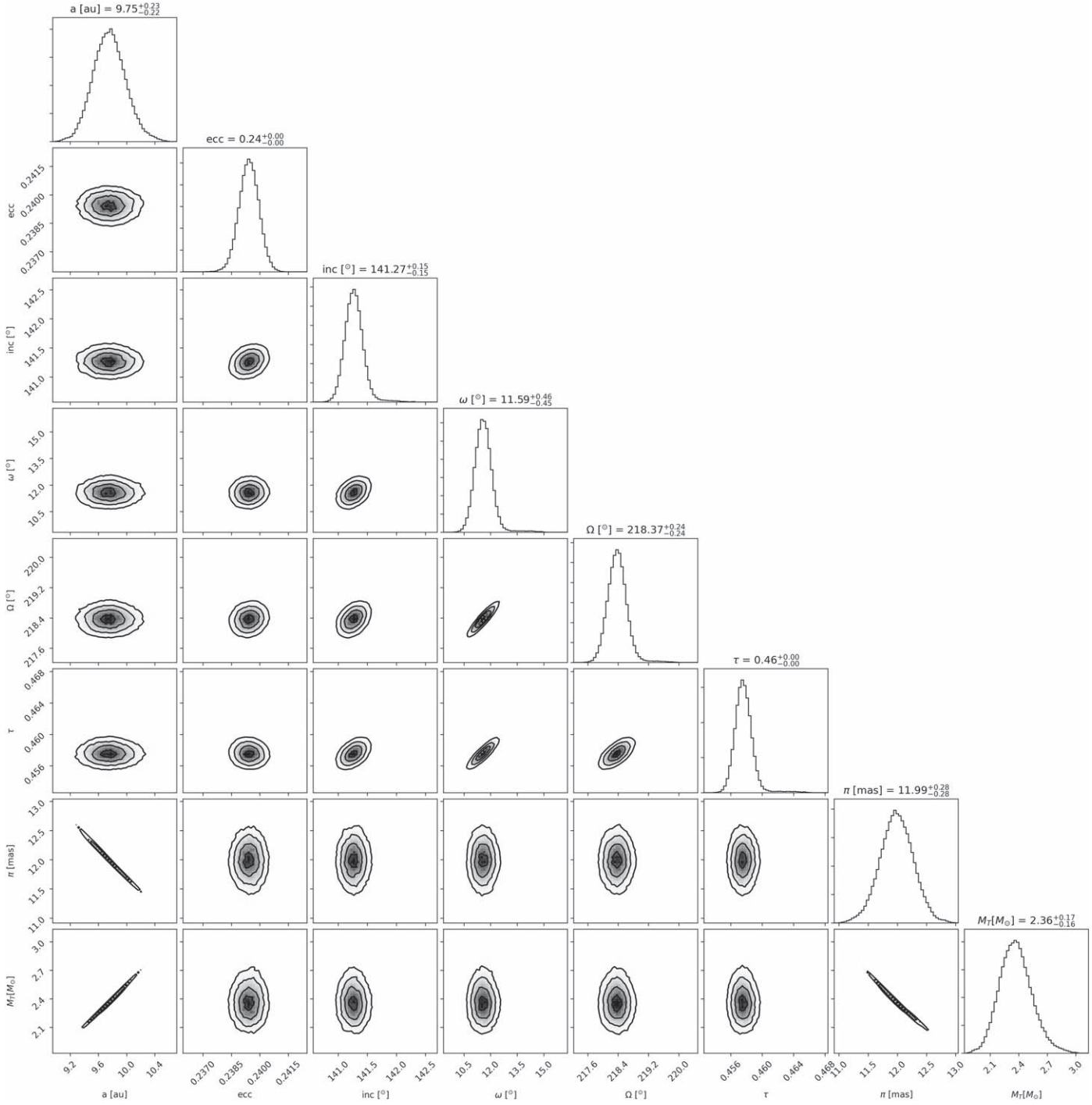

Figure 10. Corner plot of orbital parameters from the `orbitize!` fit. Uniform 2D Gaussians indicate convergence.

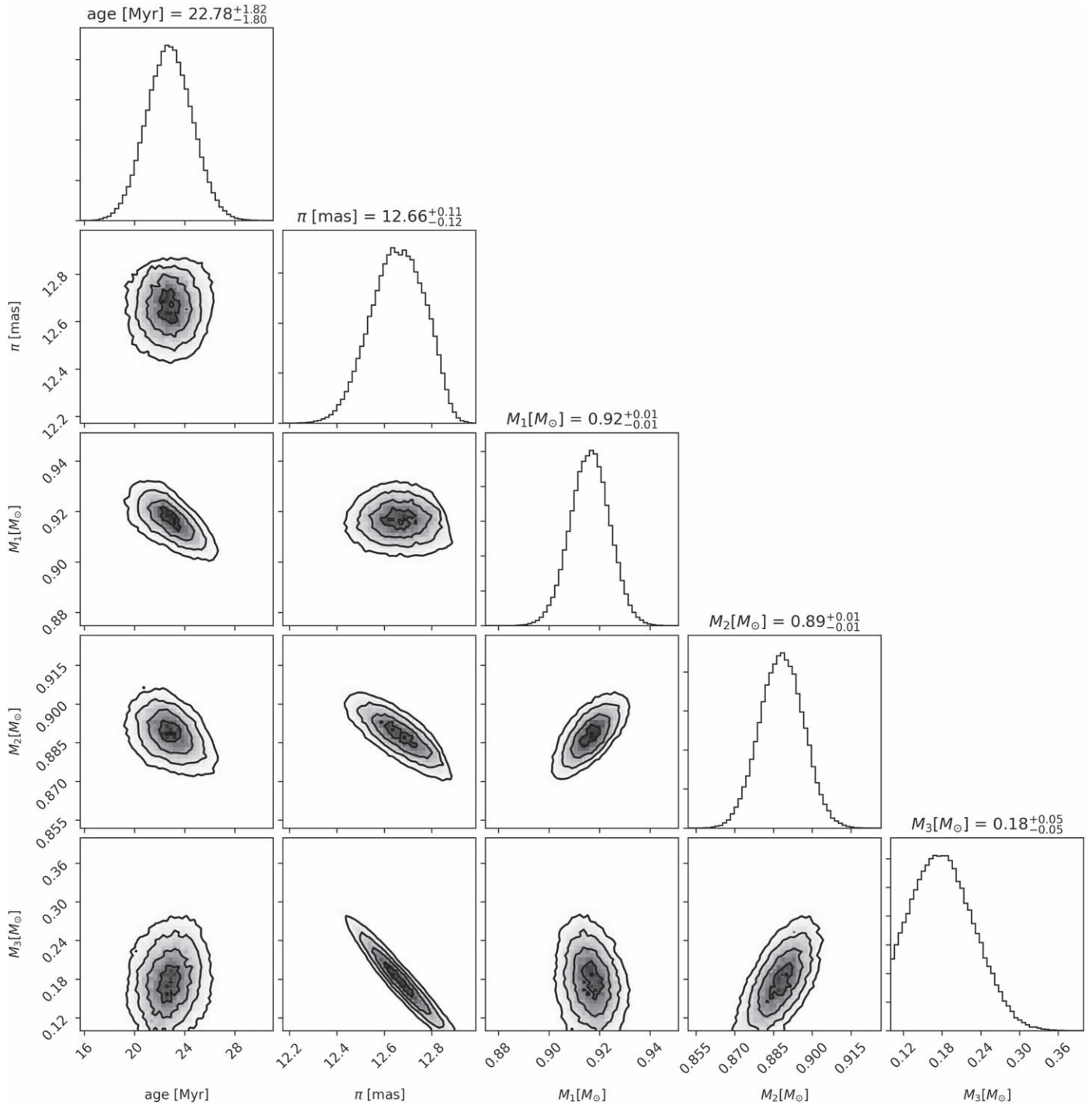

Figure 11. Covariance between the system age and parallax, and the masses of the three components derived from the MCMC analysis using the Padova PARSEC evolutionary model with a flat prior on the parallax.

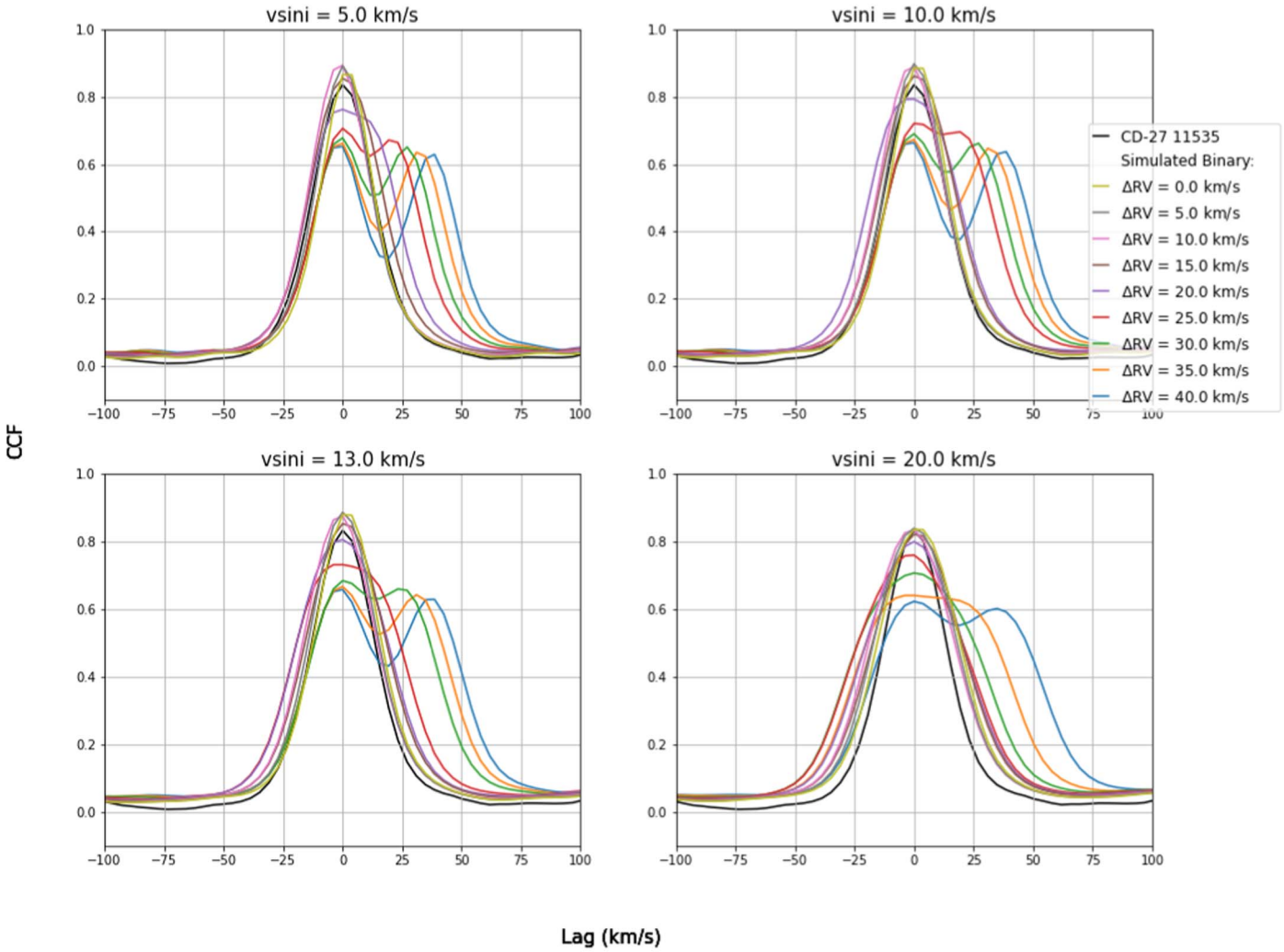

Figure 12. The cross-correlation function between one observed spectrum of CD-27 and the spectrum of HIP 41277, a single star with a similar spectral type, is shown in black and has a single peak. For all ARCES observations of CD-27, the cross-correlation yields similar results. Cross-correlation functions between a simulated binary and HIP 41277 are shown as colored curves. The different colors represent different delta RVs between A and B. For each panel, we apply a different $v \sin i$ to the components of the simulated binary. Each cross-correlation function is recentered at zero to better compare each curve. Two peaks are visible for larger delta RVs ($\gtrsim$30 km s^{-1}) when $v \sin i = 13$ km s^{-1}. The largest delta RV that produces a single peak matching the CD-27 cross-correlation function corresponds to an orbit of Ab around Aa with a semimajor axis larger than 0.04 au.

ORCID iDs

Andrew D. Thomas https://orcid.org/0000-0002-0154-5809
Eric L. Nielsen https://orcid.org/0000-0001-6975-9056
Robert J. De Rosa https://orcid.org/0000-0002-4918-0247
Anne E. Peck https://orcid.org/0000-0003-2461-6881
Bruce Macintosh https://orcid.org/0000-0003-1212-7538
Jeffrey Chilcote https://orcid.org/0000-0001-6305-7272
Paul Kalas https://orcid.org/0000-0002-6221-5360
Jason J. Wang https://orcid.org/0000-0003-0774-6502
Sarah Blunt https://orcid.org/0000-0002-3199-2888
Alexandra Greenbaum https://orcid.org/0000-0002-7162-8036
Quinn M. Konopacky https://orcid.org/0000-0002-9936-6285
Michael J. Ireland https://orcid.org/0000-0002-6194-043X
Peter Tuthill https://orcid.org/0000-0001-7026-6291
Kimberly Ward-Duong https://orcid.org/0000-0002-4479-8291
Lea A. Hirsch https://orcid.org/0000-0001-8058-7443
Ian Czekala https://orcid.org/0000-0002-1483-8811
Franck Marchis https://orcid.org/0000-0001-7016-7277
Christian Marois https://orcid.org/0000-0002-4164-4182
Max A. Millar-Blanchaer https://orcid.org/0000-0001-6205-9233
William Roberson https://orcid.org/0009-0008-9687-1877
Adam Smith https://orcid.org/0000-0002-9156-9651
Hannah Gallamore https://orcid.org/0009-0000-8603-169X
Jessica Klusmeyer https://orcid.org/0000-0003-3906-9518

References

Alonso-Floriano, F. J., Caballero, J. A., Cortés-Contreras, M., Solano, E., & Montes, D. 2015, A&A, 583, A85
Baraffe, I., Homeier, D., Allard, F., & Chabrier, G. 2015, A&A, 577, A42
Bell, C. P. M., Mamajek, E. E., & Naylor, T. 2015, MNRAS, 454, 593
Blunt, S., Nielsen, E. L., De Rosa, R. J., et al. 2017, AJ, 153, 229
Blunt, S., Wang, J. J., Angelo, I., et al. 2020, AJ, 159, 89
Bonavita, M., Gratton, R., Desidera, S., et al. 2022, A&A, 663, A144
Bressan, A., Marigo, P., Girardi, L., et al. 2012, MNRAS, 427, 127
Burgasser, A. J., & Blake, C. H. 2009, AJ, 137, 4621
Carlos, M., Nissen, P. E., & Meléndez, J. 2016, A&A, 587, A100
Chauvin, G., Vigan, A., Bonnefoy, M., et al. 2015, A&A, 573, A127
Correia, S., Richichi, A., & Schöller, M. 2003, Ap&SS, 286, 191
Cutri, R. M., Skrutskie, M. F., van Dyk, S., et al. 2003, VizieR Online Data Catalog: 2MASS All-Sky Catalog of point sources
De Rosa, R. J., Nguyen, M. M., Chilcote, J., et al. 2020, JATIS, 6, 015006
Ehrenreich, D., Lagrange, A. M., Montagnier, G., et al. 2010, A&A, 523, A73
Elliott, P., Bayo, A., Melo, C. H. F., et al. 2014, A&A, 568, A26
Elliott, P., Huélamo, N., Bouy, H., et al. 2015, A&A, 580, A88
Foreman-Mackey, D., Hogg, D. W., Lang, D., & Goodman, J. 2013, PASP, 125, 306
Gaia Collaboration, Brown, A. G. A., Vallenari, A., et al. 2018, A&A, 616, A1
Gaia Collaboration, Brown, A. G. A., Vallenari, A., et al. 2021, A&A, 649, A1
Greenbaum, A. Z., Cheetham, A., Sivaramakrishnan, A., et al. 2019, AJ, 157, 249
Høg, E., Fabricius, C., Makarov, V. V., et al. 2000, A&A, 355, L27
Kiraga, M. 2012, AcA, 62, 67
Lenzen, R., Hartung, M., Brandner, W., et al. 2003, Proc. SPIE, 4841, 944
Macintosh, B., Graham, J. R., Ingraham, P., et al. 2014, PNAS, 111, 12661
Maire, J., Ingraham, P. J., De Rosa, R. J., et al. 2014, Proc. SPIE, 9147, 85
Montet, B. T., Bowler, B. P., Shkolnik, E. L., et al. 2015, ApJL, 813, L11
Nielsen, E. L., De Rosa, R. J., Wang, J., et al. 2016, AJ, 152, 175
Perrin, M. D., Maire, J., Ingraham, P., et al. 2014, Proc. SPIE, 9147, 91473J
Rousset, G., Lacombe, F., Puget, P., et al. 2003, Proc. SPIE, 4839, 140
Schlieder, J. E., Skemer, A. J., Maire, A.-L., et al. 2016, ApJ, 818, 1
Service, M., Lu, J. R., Campbell, R., et al. 2016, PASP, 128, 095004
Shkolnik, E. L., Allers, K. N., Kraus, A. L., Liu, M. C., & Flagg, L. 2017, AJ, 154, 69
Siess, L., Dufour, E., & Forestini, M. 2000, A&A, 358, 593
Song, I., Zuckerman, B., & Bessell, M. S. 2012, AJ, 144, 8
Soubiran, C., Jasniewicz, G., Chemin, L., et al. 2013, A&A, 552, A64
Spada, F., Demarque, P., Kim, Y.-C., & Sills, A. 2013, ApJ, 776, 87
Stanford-Moore, S. A., Nielsen, E. L., De Rosa, R. J., Macintosh, B., & Czekala, I. 2020, ApJ, 898, 27
ten Brummelaar, T. A., McAlister, H. A., Ridgway, S. T., et al. 2005, ApJ, 628, 453
Tokovinin, A., Mason, B. D., Hartkopf, W. I., Mendez, R. A., & Horch, E. P. 2018, AJ, 155, 235
Tokovinin, A., Mason, B. D., Mendez, R. A., et al. 2021, AJ, 162, 41
Tokovinin, A., Mason, B. D., Mendez, R. A., & Costa, E. 2022, AJ, 164, 58
Tokovinin, A., Mason, B. D., Mendez, R. A., Costa, E., & Horch, E. P. 2020, AJ, 160, 7
Tokovinin, A., Mason, B. D., Mendez, R. A., Horch, E. P., & Briceñ o, C. 2019, AJ, 158, 48
Torres, C. A. O., Quast, G. R., da Silva, L., et al. 2006, A&A, 460, 695
Wang, S.-i., Hildebrand, R. H., Hobbs, L. M., et al. 2003, Proc. SPIE, 4841, 1145
Weise, P., Launhardt, R., Setiawan, J., & Henning, T. 2010, A&A, 517, A88
Wielen, R. 1996, A&A, 314, 679
Yelda, S., Lu, J. R., Ghez, A. M., et al. 2011, ApJ, 726, 114
Zuckerman, B., & Song, I. 2004, ARA&A, 42, 685
Zuckerman, B., Song, I., Bessell, M. S., & Webb, R. A. 2001, ApJL, 562, L87